Electronic Supplementary Material (ESI) for Environmental Science: Nano.

Supporting Information

Engineered zinc oxide-based nanotherapeutics boost systemic antibacterial efficacy against phloem-restricted diseases

Mikhael Soliman[1,2,°], Briana Lee[1,°], Ali Ozcan[1,3,‡,δ], Takat B. Rawal[4,5,#,δ], Mikaeel Young[1,6], Hajeewaka C. Mendis[1,7], Parthiban Rajasekaran[1], Torus Washington II[1], Sai Venkatesh Pingali[8], Hugh O'Neill[5,8], Andre Gesquiere[1,3], Leonardo De La Fuente[7], Loukas Petridis[4,5], Evan Johnson[9], James Graham[9], Swadeshmukul Santra[1,2,3,6]*, Laurene Tetard[1,10]*

[1] NanoScience Technology Center, University of Central Florida, Orlando, FL, 32826, USA
[2] Department Material Science Engineering, University of Central Florida, Orlando, FL, 32816, USA
[3] Department of Chemistry, University of Central Florida, Orlando, FL 32816, USA
[4] UT/ORNL Center for Molecular Biophysics, Oak Ridge National Laboratory, Oak Ridge, TN, 37830
[5] Department of Biochemistry and Cellular and Molecular Biology, University of Tennessee, Knoxville,
[6] Burnett School of Biomedical Sciences, University of Central Florida, Orlando, FL 32816, USA
[7] Department of Entomology and Plant Pathology, Auburn University, Auburn, AL 36849
TN, 37996
[8] Neutron Scattering Division, Oak Ridge National Laboratory, Oak Ridge, TN, 37830
[9] Citrus Research and Education Center, University of Florida, Lake Alfred, Florida 33850, USA
[10] Department of Physics, University of Central Florida, Orlando, FL 32816, USA
[°] Equal contributions
[δ] Equal contributions
[‡] Present address: Vocational School of Technical Sciences, Karamanoglu Mehmetbey University, Karaman, 70200, Turkey
[#] Present address: Department of Physics, University of Houston, Houston, TX, 77204

*Corresponding authors: swadeshmukul.santra@ucf.edu; laurene.tetard@ucf.edu

1. Synthesis of Zinkicide®

Zinkicide® was synthesized in a controlled chemical environment using a soluble zinc source (zinc nitrate), a surface capping agent and an oxidizing agent to control the nanoparticles. The components were mixed at room temperature for about 24 h, after which the pH was adjusted to about 7.5 with NaOH.(1)

2. Greenhouse and field trials

Citrus canker Citrus trees infected by canker disease exhibit distinctive lesions on their stems, leaves and fruits. Initially, canker is mostly limited to cosmetic blemishes, but can make the fruits unsightly, thus reducing the amount of crop available for sale. Severe infection is accompanied by early leaf and fruit drops, which significantly affect yield. Canker is caused by the *Xanthomonas citri* subsp. *citri* (Xcc) bacteria, which remain at the surface of the plant and can ooze from the lesion to contaminate surrounding trees. It can be spread by environmental factors (wind, rain) and human activity (tools, skin contact, clothing, etc). It is particularly problematic in regions with warm weather and regular rainfall or storms, such as in Florida. Canker is endemic in most of Florida. Copper products have been determined to be the most efficient to control canker, especially to avert fruit infection. For crops that are highly susceptible to canker infection, such as oranges, repeated sprays are recommended during the April-July period.(2)

Citrus greening disease Citrus trees suffering from greening disease, also known as Huanglongbing (HLB) or yellow dragon disease, see their phloem infected by *Candidatus* Liberibacter asiaticus (*C*Las), which results in decline in tree health accompanied by severe nutrient deficiencies, and significant yield losses within a few years from infection. Citrus greening constitutes a serious threat to the industry worldwide, with important losses reported in Asia, Africa, North and South America. Management of this disease is difficult and costly. Efforts have mostly been focused on limiting the spread of the disease and the decay in trees' health. In the short term, supplementing the nutrition of the trees is one focus of research as well as bactericides. Most bactericides being topical and not systemic has been found to limit the benefits observed by the infected trees. Other solutions have been considered such as heat treatments of the trees (or thermotherapy) and means to deter psyllids, the vectors of the disease, from approaching the trees. The primary long term solution envisioned to save the citrus industry is to develop genetically modified trees resistant to the disease, though research in this direction is expected to take years.(3)

3. Zinkicide® characterization

Zinkicide® characterization is challenging due to the small diameter of the individual nanoparticles, expected to be below 5 nm. Though electron microscopy is the most conventional tool for determining the shape of nanoparticles, drying caused aggregation the Zinkicide® formulation. Hence, we used SEM to assess the morphology and shape of the agglomerates. The size of individual nanoparticles in Zinkicide® was better captured with transmission electron microscopy (TEM, see Fig. 2), despite the aforementioned challenges.

Scanning electron microscopy (SEM)

SEM was used to determine the morphology of nanoparticles (Fig. S1) and to screen for the presence evaluate the presence of Zinc in the various plant tissues.

SEM images were collected for as-synthesized Zinkicide® suspensions by drop-casting the suspension on a substrate and gold-coating the sample for imaging (Fig. S1a,b). SEM images revealed aggregates (~20-50 nm) made of smaller spherical particles.

The nanoparticles were then isolated from excess reagents used during synthesis and were re-dispersed in water (Zinkicide® in water or washed Zinkicide®). The washed suspension was drop casted on the substrate, dried, and gold-coated for imaging. The corresponding SEM images (Fig. S1c,d) show that by removing the reagents from the suspension, aggregation was worsened, instigating the formation of larger aggregates (~200 nm), as shown in Fig. S1d and in Fig. S1b. This is due to the removal of reagents used to keep the nanoparticles dispersed.

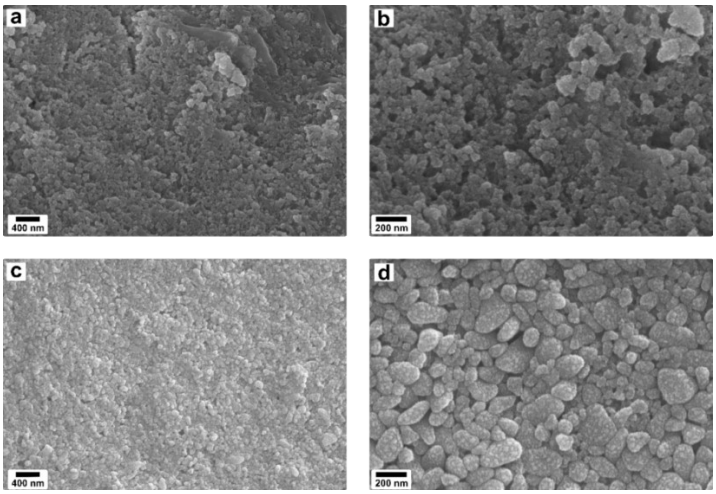

Figure S1. SEM images of as-synthesized Zinkicide® (a, b) and washed Zinkicide® (c,d). Images on the right (b.d) correspond to higher resolution views of the nanoparticles in large aggregates.

Transmission electron microscopy (TEM)

TEM measurements were carried out on freshly synthesized Zinkicide® solutions. High resolution images revealed single nanoparticles, as seen in the circles in Fig. 2b and more clearly in Fig. S2. The FFT of the TEM image (Fig. 2c) indicated the presence of crystalline orientations corresponding to ZnO in the Wurtzite phase (JCPDS #36-1451) (Table S1). Single nanoparticles were found to be spherical and ~ 5 nm in diameter (Fig. S2) with atomic planes ~2.5 Å apart (d-spacing).

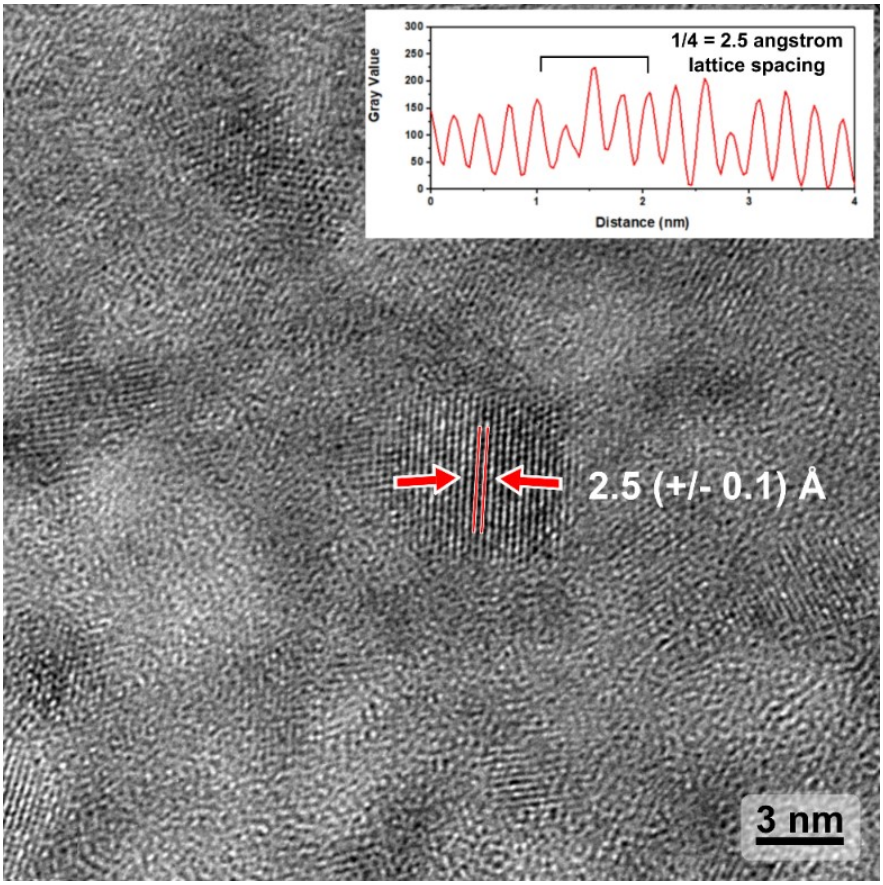

Figure S2. HRTEM image of ultra-small crystalline nanoparticles with diameter between 2.5 and 6 nm. Lattice spacing analysis (inset) indicates a lattice spacing of ~ 2.5 Å.

Table S1. Assignment of lattice spacing observed in the FFT of the TEM images (Fig. 2c).

Miller Indices (h k l)	Lattice spacing reported for ZnO Wurtzite (JCPDS #36-1451) (nm)	Lattice spacing calculated via FFT from the TEM images (nm)
(1 0 3)	1.48	1.46
(1 1 0)	1.62	1.63
(1 0 2)	1.91	1.91
(1 0 1)	2.48	2.46
(1 0 0)	2.81	2.81

Neutron scattering

The structure of an individual Zinkicide® particle in aqueous solvent was investigated using small-angle neutron scattering (SANS).

Usually, a "dilute" concentration of such core-shell particles is measured to eliminate *inter-particle correlations* and only be sensitive to the internal structure of these particles. However, due to the small size (< 5 nm dia.) of the Zinkicide® particles, our ability to resolve the core-shell structure in the dilute concentration regime proved unsuccessful. Therefore, these reported measurements were performed on a high concentration of Zinkicide® particles ~ 1000 mg/mL and were further combined with contrast variation to resolve the core-shell structure of the Zinkicide® particles. A high concentration of the Zinkicide® particles exhibited a hierarchical scattering profile, i.e., the scattering intensity continuously increases with decreasing Q over multiple length scales (Fig. 2d) because the close packing of the primary particles promotes the formation of agglomerates too. Nevertheless, the most notable feature was found in the high-Q region (> 0.1 $Å^{-1}$) and is related to the Zinkicide® primary particle shape, size and a low degree of order in the arrangement of these particles.

The SANS data was analyzed using the multi-level Unified Fit implemented in the Irena Package(4) to elucidate the multiple levels of structural organization of these hierarchical systems. For each individual level, *i*, the scattering signal is the sum of Guinier's exponential form and the structurally limited power-law as:(5, 6)

$$I(Q) = \sum_{i=1}^{n}\left[G_i exp\left(-Q^2 R_{g_i}^2/3\right) + B_i exp\left(-Q^2 R_{g_{(i+1)}}^2/3\right)\left\{\left[erf\left(QR_{g_i}/\sqrt{6}\right)\right]^3/Q\right\}^{P_i}\right] + I_{bkg} \quad (1)$$

where i=1, …, n. A total of 3 levels were employed with levels i=1 and i=3 referring to the smallest and largest-size structural levels, respectively. $G_i = c_i V_i (\Delta\rho_i)^2$ is the exponential prefactor; R_{g_i} is the radius of gyration describing the average size of the i^{th} level structural unit; B_i is a Q-independent prefactor specific to the type of power-law scattering with power-law exponent P_i, and I_{bkg} is the flat background intensity due to incoherent scattering. c_i is the concentration of the i^{th} kind of particle; V_i is the volume of the particle

and $\Delta\rho_i$ is the contrast of the i^{th} kind of particle with respect to the solvent. The expression of the constant prefactor is $B_i = \left(G_i P_i / R_g^{P_i}\right)\Gamma(P_i/2)$ when the i^{th} level is a mass fractal composed of elementary units of the lower, $(i\text{-}1)^{th}$, level. The radius of gyration parameter obtained from level-1 represents the smallest particle size in the system and is converted to the diameter of the spherical particles by multiplying with a factor of ~2.6. Inter-particle interactions between spherical particles were modelled using spherical correlations- $I(Q) = I(Q)/[1 + pf(Q\eta)]$, where p is the packing factor, $f(Q\eta)$ is the sphere amplitude for the spherical correlations and η is the inter-particle correlation distance.

The most relevant structural parameter is the primary particle diameter obtained from the high-Q region of the data. The Unified fit represents primary Zinkicide® particle features in level-1 and the agglomerates of these particles in levels 2 and 3 (Table S2 level-1). To elucidate the structure of individual Zinkicide® particles, level-1 component of the Unified fit is the only relevant information from the fit and in particular, the parameters, R_g and η (bold numbers in Table S2). Irrespective of the contrast (0% or 42% D_2O solvent), the inter-particle distance is expected to be the same for the same packing density, which is consistent with our results (η = 27 Å). While the average size of the particle (R_g , which was converted to particle diameter, D (in Angstroms) assuming the particles are spherical) depends on the contrast between the shell and solvent. In 0% D_2O solvent, the entire particle size is measured (R_g ~ 11.9 Å or d = 30.7 Å) and in 42% D_2O solvent, due to a lower contrast between shell and solvent, a slightly smaller particle size was observed (R_g ~ 11.5 Å or d = 29.7 Å). Furthermore, the shell thickness on these particles can be estimated from comparing the results of particle size (d) and the inter-particle distance (η). Because the shell region is penetrable, η provides a measure of the core diameter, while d in 0% D_2O provides the upper limit on the entire particle size. This implies that the average size of the core of the Zinkicide® particles are 27 Å and the shell thickness is at most 4 Å.

Table S2. Fitting parameters of the 3-level Unified fit model used for fitting SANS data.

As-synthesized Zinkicide® c = 1000 mg/mL	**Levels**	***G***	***R_g* (Å)**	***B***	***P***	***η* (Å)**	***p***
0% D_2O	**1**	2.4	**11.9** $^{+1.6/-1.1}$	$^{\#}$5.5 E–4	4.0	**27** $^{\pm 3}$	1.3 $^{+1.1/-0.5}$
	2	286	144	$^{!}$11.9	2.9		
	3	1.3 E+5	1185	$^{!}$8.3	3.0		
42% D_2O	**1**	0.7	**11.5** $^{+4/-1.6}$	$^{\#}$2.0E–4	4.0	**27** $^{+8/-4}$	1.2 $^{+2.4/-0.6}$
	2	188	173	$^{!}$14.9	3.0		
	3	2.1 E+5	1738	$^{!}$10.0	3.2		

$^{\#}$ linked to G/Rg/P

$^{!}$ Degree of Aggregation (for mass fractals)

Raman spectroscopy

The Raman signatures of as-synthesized Zinkicide® and Zinkicide® in water (washed) are presented in the manuscript (Fig. 2e):

- **sodium salicylate:** 818 cm^{-1} bending mode of C-C, 1020 cm^{-1} in-plane bending mode of C-H, 1260 cm^{-1} stretching mode of C-O in hydroxyl group, 1390 cm^{-1} stretching mode of C-O in carboxyl group, 1460 cm^{-1} stretching mode of C-C, 1630 cm^{-1} stretching mode of C=O, and 3070 cm^{-1} stretching mode of C-H)(7)
- **nitrate from the Zn nitrate source:** 1050 cm^{-1} and 1360 cm^{-1} symmetric and antisymmetric stretching modes of the nitrate ion, respectively(8)
- **hydrogen peroxide:** 870 cm^{-1} stretching mode of O-O.(9)

After removing excess reagents, a band at 840 cm^{-1} was observed in lieu of all the aforementioned bands. Raman spectroscopy was also used the assess the change in composition in leaves and stems of treated seedlings. Fig. S3 indicates the Raman fingerprint of the liquid extracted from untreated control leaves (bottom) and treated leaves collected in the lower (middle) and upper (top) parts of the seedling. Signature corresponding to nitrate was present after treatment, suggesting movement of the reagents in the plant. However, the nanoparticle movement could not be assessed from this data.

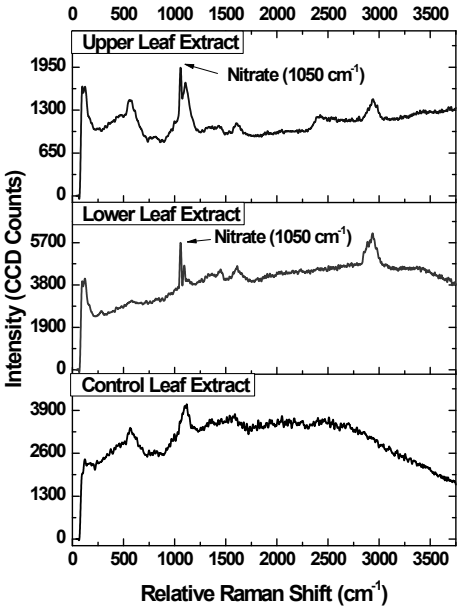

Figure S3. Raman spectra of exudate from leaves collected on seedlings. Plants exposed to Zinkicide® exhibit a high intensity narrow band at ~1050 cm^{-1}, corresponding to the presence of nitrate.

4. Computational studies

Bulk ZnO_2

ZnO_2 is a pyrite-like structure that crystallizes in a simple cubic unit cell (crystallographic space group $Pa\bar{3}$), which is made of four Zn atoms and eight O atoms (Fig. S4a), with each Zn bonded to six equivalent O atoms to form an octahedron (Fig. S4b). We modeled three bulk systems of increasing size: (1x1) unit cell, (2x2) and (3x3) cells, for which we used the 11x11x11, 5x5x5, and 2x2x2 k-point mesh with the automatic generation of k points within the Monkhorst-Pack scheme(10) for sampling the Brillouin zone (BZ), respectively. The coordinates of all atoms of the bulk model systems were relaxed using the Broyden–Fletcher–Goldfarb–Shanno (BFGS) quasi-newton algorithm until the energy converged below 10^{-7} Ry and the residual force on each atom reached below 10^{-5} Ry/a.u. The gamma point frequencies for the relaxed structures were obtained using the linear response approach within density functional perturbation theory.(11, 12) The DFT-optimized lattice constants for ZnO_2 bulk (1x1) unit cell were: a = b = c = 4.861 Å.

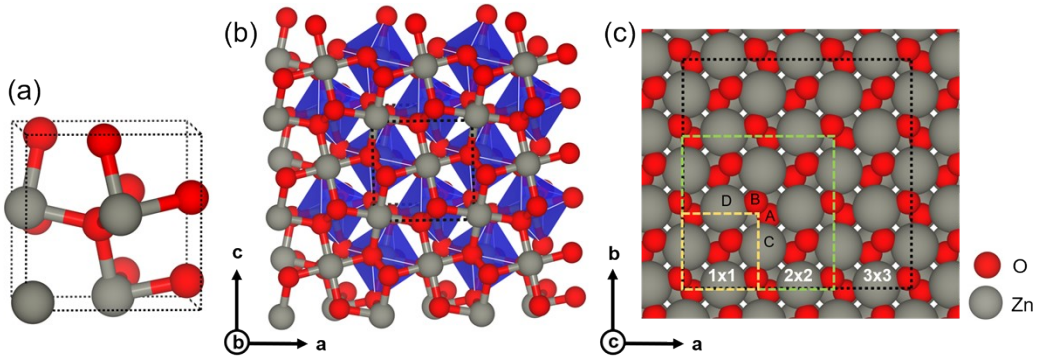

Figure S4. a, Unit cell of ZnO_2. Oxygen is shown in red and Zinc in grey; **b,** the ZnO_2 crystal structure, indicating its polyhedral structure, in which each Zn atom is bonded with six O atoms forming an octahedron; **c,** schematic representation of (1x1), (2x2) and (3x3)-ZnO_2(100) surface unit cell, as indicated by the yellow, green, and black-colored dashed lines.

ZnO_2(100) surface

For the DFT optimized ZnO_2 bulk structure, the (100) surface was cut normal to the z axis of the crystalline structure, while keeping the periodicity along x and y axis. To mimic a surface, we added a vacuum of 15 Å along the z axis to prevent spurious electrostatic interactions between the periodical same images. We constructed ZnO_2(100) slabs of increasing system size: (1x1) containing 24 O atoms and 12 Zn atoms and (2x2) containing 96 O atoms and 48 Zn atoms.

For (2x2) supercell geometry, the surface O_2 are approximately aligned along the diagonal of two axes represented by vectors **a** and **b** (Fig. S4c). After relaxation, the Z position of the two O atoms (called

here O_A and O_B, refer Fig. S4c) was not the same, as indicated by the calculated angels between Zn and the two O atoms, i.e. Zn_C-O_A-O_B = 112° whereas Zn_D-O_B-O_A = 106° (refer Zn_C and Zn_D in Fig. S4c). The calculated O_A-O_B distance was found to be 1.49 Å, while the O-Zn distance varied: O_A-Zn_C = 2.10 Å and O_B-Zn_D = 2.04 Å. Such difference in surface O-Zn distances can be attributed to the asymmetric coordination of the O_A and O_B atoms. A surface O_A is coordinated with two surface Zn atoms and an inner Zn atom, whereas a surface O_B is coordinated with two surface Zn atoms and an O_A atom.

Next, two surface O atoms per (1x1) unit cell were removed to make the non-stoichiometry composition, which was found to help achieve the stable surface. It was considered here to represent the oxygen-deficient ZnO_2 surface. The final structural models of (1x1) and (2x2) supercell contain 22 O atoms and 12 Zn atoms, 88 O atoms and 48 Zn atoms, respectively. We used the 11x11x1 and 5x5x1 k-point mesh with the automatic generation of k points within the Monkhorst-Pack scheme(10) for the integration of the BZ of (1x1) and (2x2) cells, respectively. The atoms of these unit cells were relaxed with the same criteria for energy and force convergence. However, a Gaussian smearing of width 0.1 eV (0.008 Ry) was used for smooth energy convergence.

ZnO_2(100)/ZnO(10-10) system

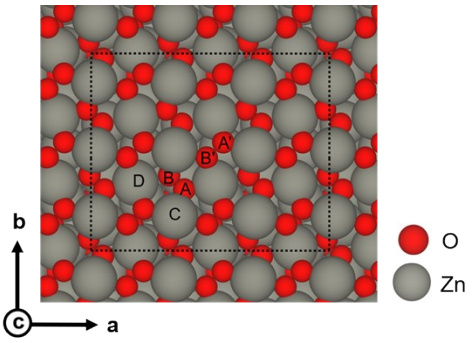

Figure S5. DFT-optimized structure of the hybrid ZnO_2/ZnO shell-core system (top view). The supported ZnO_2 unit cell is represented by black dotted lines (square shape). The O_2, i.e. O_2(A-B)) in the case of the ZnO_2(100) surface, is now embedded by surface Zn atoms, owing to interaction with the ZnO slab. Note that the shape of the supported 3x3 ZnO_2 monolayer is not the same as unsupported (3x3) ZnO_2(100) unit cell since to form the hybrid shell-core system, their interface should minimize the lattice mismatch. The labels are given for referring atoms, whose distances and angles are described in the text.

A heterostructure model system of ZnO_2 and ZnO was constructed using a monolayer of (3x3)-ZnO_2 that was supported by the (3x4)-ZnO(10-10) slab, to mimic a shell-core nanoparticle with ZnO as the core and ZnO_2 monolayer as the outer surface. The lattice mismatch at the interface between ZnO_2 and the ZnO

along the x,y directions was determined here as the difference in magnitude of their lattice vectors, $\vec{a}$ and $\vec{b}$, which were found to be 3.8% and 2.7%, respectively. For the relaxation of the (3x3)-ZnO_2(100)/(3x4)-ZnO(10-10) model, only one k point was used for sampling BZ to minimize the computational cost arising from the calculations associated with the interfacial structure complexity. The geometries of the hybrid ZnO_2/ZnO system were optimized using the BFGS quasi-newton algorithm until the energy converged below 10^{-5} Ry and the residual force on each atom reached below 10^{-3} Ry/a.u. The schematic representation of the optimized structure is shown in Fig. S5.

For (3x3) ZnO_2(100) supported on the (3x4) ZnO(10-10), the surface O_2, i.e. O_2(A-B), which was originally aligned along the diagonal of the two lattice vectors, $\vec{a}$ and $\vec{b}$, was found to be slightly embedded inside the surface Zn atoms (Fig. S5) owing to the fact that surface Zn atoms were displaced up along z axis. The calculated surface $O_{A'}$-$O_{B'}$ distance was found to 1.51 Å, elongated by 0.02 Å as compared to the surface O_2 of the unsupported ZnO_2(100), whereas the O_A-O_B distance of the embedded O_2 of the supported monolayer ZnO_2 was 1.50 Å. The calculated O_A-Zn_C distance was found to 1.89 Å, while the O_B-Zn_D distance was 2.32 Å, thus indicating the substantial relaxation of surface Zn and O atoms.

To model a defective surface, one O_2 was removed from the surface of the supported ZnO_2. The geometries of the defective ZnO_2/ZnO system were optimized with the same criteria described above. The resulting defective ZnO_2/ZnO system was used for investigating the adsorption of H_2O as well as the formation of reactive oxygen species (ROS) on the surface. The ZnO_2/ZnO systems with different adsorbates (H_2O, O_2, OOH, OH) were relaxed with the same criteria mentioned above. To model the co-adsorption of H_2O and O_2 in the presence of defects, we placed the O_2 in the oxygen vacant sites, and the H_2O at the nearest Zn site. Similarly, we modeled the co-adsorption of OOH and OH by placing them at the half lattice spacing away and full lattice spacing away from the defects, respectively, along $\vec{b}$ (y axis). We labeled adsorbed species with an asterisk (*).

Vibrational frequencies of ZnO_2 bulk, ZnO_2 surface, and ZnO_2/ZnO

For ZnO_2 bulk, the calculated O-O stretching frequencies were: 1005 cm^{-1}, 873 cm^{-1}, and 866 cm^{-1} for (1x1), (2x2), and (3x3) supercell, respectively (Table S3). Thus, increasing the supercell beyond (2x2) was not found to significantly affect the calculated frequency. For the ZnO_2(100) surface, the O-O stretching frequency of the surface O_2 moiety were found to be 948 cm^{-1} and 860 cm^{-1} for the (1x1) and (2x2) supercell, respectively. These calculations indicate that for similar size along x and y, the O-O stretching frequency of the ZnO_2(100) surface is slightly smaller than that of bulk ZnO_2. For the hybrid ZnO_2/ZnO system, the stretching frequency was 837 cm^{-1}. The ZnO_2/ZnO shell-core model is thus found in good agreement with the Raman spectroscopy measurements (840 cm^{-1}).

Table S3. Results of DFT calculations and of Raman spectroscopy.

Structural Models	Number of atoms	O-O stretching frequency (cm^{-1})	O-O bond length (Å)
ZnO_2 bulk	96	873	1.46
ZnO_2(100) surface	136	860	1.49
ZnO_2/ZnO shell-core	198	837	1.51
Raman (this work)		840	-

Interaction of H_2O, OOH and OH with shell-core system

We first discuss the adsorption of a H_2O molecule on the defective ZnO/ZnO_2 shell-core model in the presence of an O_2, which was found to fill the vacant sites. Fig. S6 shows a DFT-optimized configuration of one H_2O molecule adsorbed on the ZnO_2 surface of the shell-core system. H_2O was found to adsorb molecularly at a surface Zn site, whose z position was higher than the Zn atom embedded below the adsorbed O_2 at vacant sites (surface O_2). In this configuration, H_2O was found to make a hydrogen bond with O_2 (indicated by blue arrow in Fig. S6) where the H-O-H…O-O distance was 1.35 Å. The calculated closest distance between an O atom of H_2O and a surface Zn atom (adsorption site) was 1.96 Å, and the distance between an O atom of H_2O and the H atom closest to the ZnO_2, was 1.11 Å, longer than the other H_2O O-H bond of 0.97 Å. The local interaction between H_2O and surface O_2 was also found to reduce the O-O bond length from 1.51 Å to 1.48 Å.

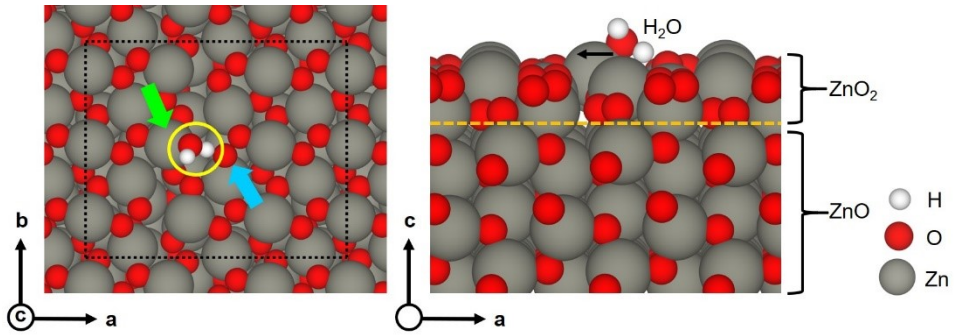

Figure S6. DFT-optimized structure of a H_2O molecule (yellow circle) molecularly adsorbed on monolayer ZnO_2 supported on ZnO(10-10): top view (left), and side view (right). The surface Zn atom that acts as an adsorption site (green arrow) undergoes significant lateral displacement, and an O atom of surface O_2 (blue arrow) is involved in hydrogen bonding with the H_2O hydrogen atom.

The adsorption of a H_2O also leads to the significant lateral displacement, by 1.10 Å, of the Zn atom at the binding site (indicated by green arrow, Fig. S6). The calculated binding energy of H_2O within the revised

vdW-DF2 level was found to be -1.68 eV, which is slightly stronger than adsorption of H_2O on the ZnO(10-10) surface (binding energy ~ -1.26 eV).(13)

Our DFT calculations indicate that the reaction $H_2O^* + O_2^* \square OOH^* + OH^*$, which has been proposed for producing ROS in the dark(14), is energetically unfavorable, whereas the process $H_2O^* + O_2^* \square OH^* + OH^* + O^*$ is favorable (see main text). The perturbation of surface O_2^* by H atoms leads to the formation of surface O* and two hydroxyl species, considered as ROS.

5. Movement of Zn in plants

Movement of the treatment was studied using both Raman spectroscopy and elemental analysis, which made it possible to monitor Zn in the plant tissues. Six-month old greenhouse Young "Bitter Orange" (*Citrus* × *aurantium*) seedlings (~ 50 cm shoot length) were used for the study. The plants were exposed to the treatment via the roots to mimic the soil drench method used in the field. We removed the soil from and thoroughly cleaned the roots using DI water before placing them into a 250 mL graduated cylinder filled with 150 mL of as-synthesized Zinkicide® (19,000 μg/mL of Zn metal). Untreated controls (UTC) were prepared similarly, however roots were submerged in DI water. Seedlings were maintained in a growth chamber (Panasonic, Newark, NJ, USA) for up to 24 h, with the temperature held between 25 °C and 31 °C, and humidity cycled between 60% and 80% to mimic conditions in Florida citrus groves. A very high concentration of Zinkicide® was purposely selected to achieve detectable Zn levels with the tools used for elemental analysis, as the intent of the study was to confirm movement of the treatment, and not to assess the level achieved in grove conditions. We note that quantifying the Zn content in trees found in groves would be more complex than this simplified model of the seedling, given the complex vascular system of mature trees, with numerous branches and different stages of leaf growth. This is outside of the scope of this work.

For SEM and EDS characterization, leaf and stem sections were collected from freeze-dried seedlings to preserve the content of the vessels. The sections were then air dried from a minimum of 24 h before being gold coated by sputtering. As shown in Fig. 4c,d the elemental analysis of the phloem and xylem confirmed the presence of Zn in the tissue, which was not present in the pith, nor in the untreated control (Fig. S7, top SEM images and black line in the EDS graph). Inspection of different sites in the leaves and stems revealed the presence of vessels filled with residues. In the case of the untreated control, an example of such residues is indicated by the orange marker on the high-resolution SEM image (top). EDS spectra acquired on these residues did not show any sign of Zn. On the other hand, residues found in the phloem and xylem of the treated seedlings exhibited signs of 100-200 nm spherical aggregates, indicated by the orange cross in the high-resolution SEM image (bottom). These residues were found to be rich in Zn, as shown in the EDS

spectrum (red curve). AAS data presented in Fig. S12 indicate that even when washing the nanoparticles in reagents 12 times, the discard does not contain high level of Zn. In this plant uptake study, the nanoparticles remained in reagent, i.e. as-synthesized Zinkicide®, in the graduated cylinder for the duration of the experiment. Once inside the plant, Raman data (Fig. 4a,b) indicates that the reagents also move in the plant. Although the environment of the nanoparticles was changing, the evidence suggests that full dissolution within the few hours of the treatment is improbable, and the locations exhibiting strong Zn content are likely indicative of the presence of Zinkicide® nanoparticles in the plant.

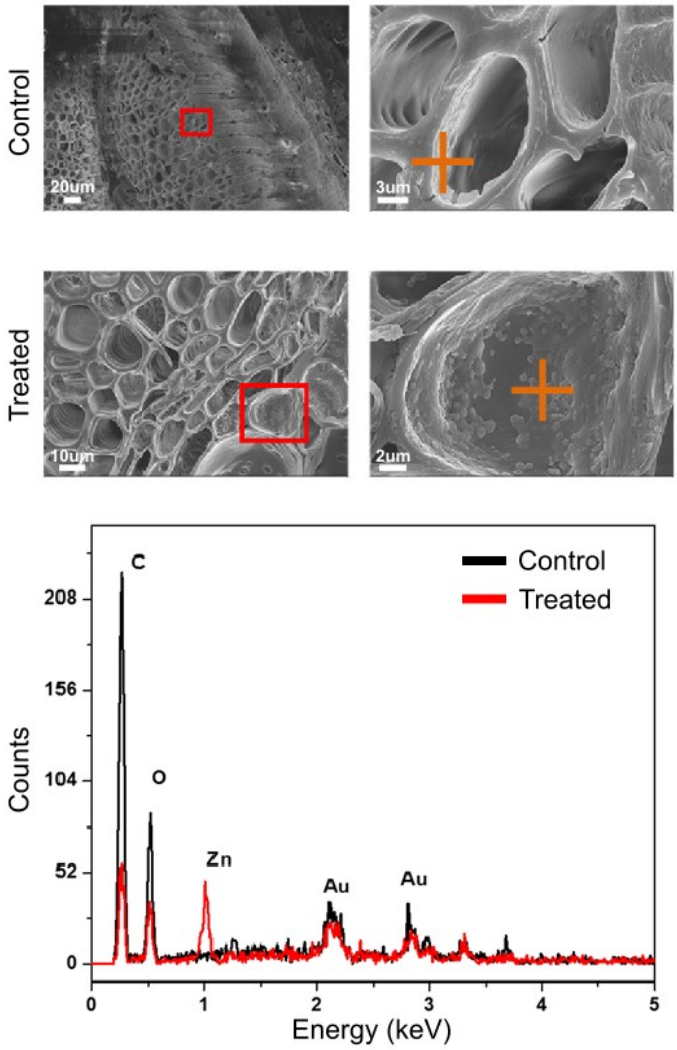

Figure S7. (left) SEM images of untreated (top) and treated (bottom) plant leaves. (right) Representative EDS spectra obtained on untreated plant (black) and on a plant treated with ZnO nanoparticles (red).

A more quantitative determination of the Zn concentration in the plant tissues was obtained with X-Ray fluorescence (XRF) spectroscopy (Fig. S8). A calibration of the XRF data was done by analyzing a set of

citrus leaves with increasing Zn content with both XRF and inductively coupled plasma - optical emission spectrometry (ICP-OES). Zn content of untreated control plants was found to be ~ 30 µg/g. In plants treated with Zinkicide® Zn content increased as early as 6 h after the beginning of the treatment, for both leaves and stems. Due to the ongoing exposure of the roots to the treatment, the level in Zn content continued to increase within 24 h of the experiment. The Zn concentration in leaves collected from the top of the seedlings was found to reach a maximum 18 h after the start of the treatment (~3500 µg/g). The overall Zn content increased in all leaves and seedlings at the 24 h time point, reaching a level close to 3000 µg/g in the leaves and 2000-4000 µg/g in the stems. The very high concentration of the treatment (19000 µg/mL) led to a Zn concentration of up to 4000 µg/g in the plant. Hence, it is plausible that the treatment concentrations used in the field could be optimized to deliver Zinkicide® above the MIC in the plant (Table 1).

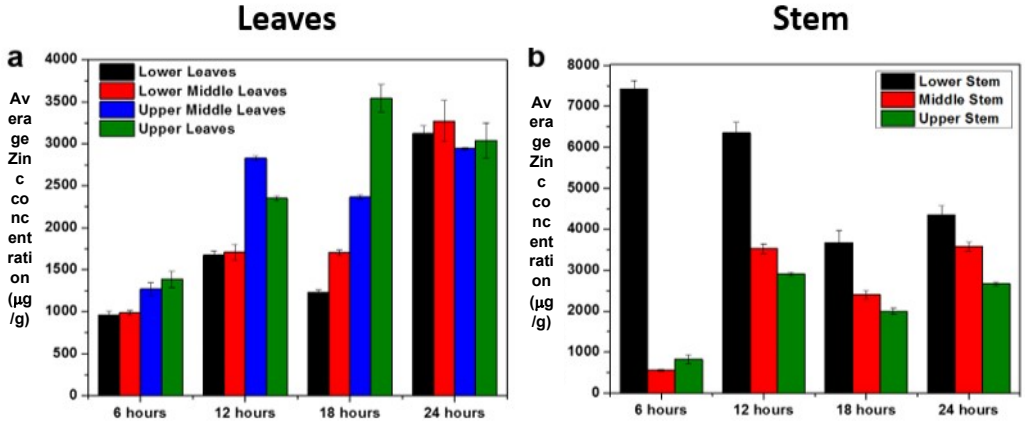

Figure S8. Average elemental Zn concentration in the leaves and stems of citrus seedling dipped in 19000 µg/mL Zinkicide® for 24 h. Concentrations were determined by XRF, which was previously calibrated by correlating peak intensities to concentrations values obtain in the same samples with ICP-OES.

6. Zinkicide®-bacteria interactions

The MIC of as-synthesized Zinkicide® is reported in Table S4. MIC and as-synthesized Zinkicide® at week 1 represent the MIC of the freshly synthesized formulation. As-synthesized Zinkicide® is comprised of ZnO nanoparticles in excess reagents. When removing excess reagents to isolate the nanoparticles (suspension referred to as 'Zinkicide® in water' or 'washed Zinkicide®') maintain most of the efficacy against *E. coli* (MIC_{washed} = 32-65 µg/mL; $MIC_{as\text{-}synthesized}$ = 9-18 µg/mL), with some loss of efficacy against *X. alfalfae* (MIC_{washed} = 130-260 µg/mL; $MIC_{as\text{-}synthesized}$ = 38 µg/mL). In all cases the MICs obtained constitute a significant improvement compared to the MICs obtained for copper hydroxide and cuprous oxide/zinc

oxide, which are considered grower standards in bacterial treatments. We note that MIC against *C*Las could not be determined due to the difficulties to grow the strain in culture *in situ*.

The evolution of the MIC values over a period of 18 weeks was also monitored. The complete data set is presented in Table S4. While the as-synthesized Zinkicide® retained a MIC below 36 µg/mL against *E. coli* and below 76 µg/mL against *X. alfalfae* for 18 weeks, a slight decay in efficacy was observed over time in both cases. For both *E. coli* and *X. alfalfae*, the efficacy of washed Zinkicide® was inferior to the as-synthesized formulation and had MICs which stabilized around week 8 with values comparable to copper hydroxide. The primary difference in MICs between *E. coli* and *X. alfalfae* is the variability in MICs within the first few weeks, where *X. alfalfae* experienced the most variance in week 1 versus week 2 for *E. coli*.

Table S4. Summary of MIC of Zinkicide® and controls against *E. Coli* and *X. alfalfae* evaluated between week 1 to 18.

Materials	*E. coli* (µg/mL metallic content)								
	1st Week	2nd Week	3rd Week	4th Week	6th Week	8th Week	10th Week	12th Week	18th Week
Zinkicide Unwashed	9-18	9-18	9-18	9-18	9-18	9-18	9-18	9-18	18-36
Zinkicide Washed Wk1	32-65	65-130	130-260	130-260	260	260	260	260	260
Zinkicide Washed Wk 2	-	135-270	135-270	135-270	270	270	270	270	270
Zinkicide Washed Wk 3	-	-	130-260	130-260	260	260	260	260	260
Zinkicide Washed Wk 4	-	-	-	220	220	220	220	220	220
Zinkicide Washed Wk 6	-	-	-	-	223	223	223	223	223
Zinkicide Washed Wk 8	-	-	-	-	-	249	249	249	249
Zinkicide Washed Wk 10	-	-	-	-	-	-	248	248	248
Zinkicide Washed Wk 12	-	-	-	-	-	-	-	240	240
Zinkicide Washed Wk 18	-	-	-	-	-	-	-	-	290
Copper Hydroxide	250-500	250-500	250-500	250-500	250-500	250-500	250-500	250-500	250-500
Cuprous oxide/zinc oxide	125-250 (Cu), 125-250 (Zn)	125-250 (Cu), 125-250 (Zn)	125-250 (Cu), 125-250 (Zn)	125-250 (Cu), 125-250 (Zn)	125-250 (Cu), 125-250 (Zn)	125-250 (Cu), 125-250 (Zn)	125-250 (Cu), 125-250 (Zn)	125-250 (Cu), 125-250 (Zn)	125-250 (Cu), 125-250 (Zn)

Materials	*X. alfalfae* (µg/mL metallic content)								
	1st Week	2nd Week	3rd Week	4th Week	6th Week	8th Week	10th Week	12th Week	18th Week
Zinkicide Unwashed	38	38	38	38	38-76	38-76	38-76	38-76	38-76
Zinkicide Washed Wk1	130-260	260-520	260-520	260-520	260-520	260-520	260-520	260-520	260-520
Zinkicide Washed Wk 2	-	270-540	270-540	270-540	270-540	270-540	270-540	270-540	270-540
Zinkicide Washed Wk 3	-	-	260-520	260-520	260-520	260-520	260-520	260-520	260-520
Zinkicide Washed Wk 4	-	-	-	220-440	220-440	220-440	220-440	220-440	220-440
Zinkicide Washed Wk 6	-	-	-	-	223-446	223-446	223-446	223-446	223-446
Zinkicide Washed Wk 8	-	-	-	-	-	250-500	250-500	250-500	250-500
Zinkicide Washed Wk 10	-	-	-	-	-	-	249-498	249-498	249-498
Zinkicide Washed Wk 12	-	-	-	-	-	-	-	241-582	241-482
Zinkicide Washed Wk 18	-	-	-	-	-	-	-	-	290-580
Copper Hydroxide	250-500	250-500	250-500	250-500	250-500	250-500	250-500	250-500	250-500
Cuprous oxide/zinc oxide	125-250 (Cu), 125-250 (Zn)	125-250 (Cu), 125-250 (Zn)	125-250 (Cu), 125-250 (Zn)	125-250 (Cu), 125-250 (Zn)	125-250 (Cu), 125-250 (Zn)	125-250 (Cu), 125-250 (Zn)	125-250 (Cu), 125-250 (Zn)	125-250 (Cu), 125-250 (Zn)	125-250 (Cu), 125-250 (Zn)

Cell wall degradation and damage caused by ROS is the mode of action most attributed to ZnO nanoparticles (Fig. 5a,b).(15-17) Atomic force microscopy (AFM) is suitable to determine changes in morphology and surface roughness (18-20) but lacks the chemical speciation necessary to evaluate the formation of ROS or changes in composition taking place. On the other hand, traditional oxidative stress assays require the addition of a dye that undergoes a chemical change upon interaction with ROS, resulting in a specific optical signature. This assay may suffer from limitations as nanoparticles could alter the optical property of the dye through direct interaction. Ideally the dye should react to the ROS produced by the nanoparticle but not the nanoparticle itself. However, it is challenging to rule out the possibility of direct interaction between the ROS active dye and the nanoparticle in the solution state. The nanoIR evaluation of the individual bacteria composition was used to complement the conventional bioassays (MIC, CFU) which provide information on a large number of bacteria.

Nano-IR avoids the need for chemical tagging required by fluorescence measurements and unveils the compositional changes at the individual bacterium level. Previous reports demonstrated that nano-IR is sensitive to conformational changes of proteins caused by varying treatments or conditions, which can serve as indicators of ROS damage thereby circumventing the need for dyes (21, 22).

Table S5. Assignment of IR band in the fingerprint of bacteria obtained with nanoIR measurements.

NanoIR band	**Bonds**		**Untreated**	**Copper hydroxide (Kocide)**	**Cuprous oxide /zinc oxide (Nordox)**	**Zinkicide® as-synthesized**	**Zinkicide® in water**	**Ref**
undetermined		Position Height Width			1588 cm^{-1} 5 19 cm-1	1600 cm^{-1} 26 50 cm^{-1}		
Amide I C=O	*β-sheets*	Position Height Width	1628 cm^{-1} 9 17 cm^{-1}	1620 cm^{-1} 31.5 24 cm^{-1}	1626 cm^{-1} 11 18 cm^{-1}	1631 cm^{-1} 61 11.8 cm^{-1}	1624 cm^{-1} 3 15.4 cm^{-1}	**(23, 24)**
	Random coil and/or α-helix	Position Height Width	1661 cm^{-1} 26 22.7 cm^{-1}	1659 cm^{-1} 142 26 cm^{-1}	1659 cm^{-1} 35 24 cm^{-1}	1662 cm^{-1} 117.3 20.8 cm^{-1}	1658 cm^{-1} 27.8 26.6 cm^{-1}	
	β-turns	Position Height Width	1709 cm^{-1} 5 21.5 cm^{-1}	1709 cm^{-1} 7 32 cm^{-1}	1712 cm^{-1} 3.5 32 cm^{-1}	1707 cm^{-1} 16.7 20 cm^{-1}	1712 cm^{-1} 0.1 15 cm^{-1}	

7. Evolution of ZnO nanoparticles overtime

Dynamic light scattering (DLS) is commonly used to determine the hydrodynamic diameter of nanoparticles. DLS measurements returned readings in the 135-200 nm range (Fig. S9), which correspond

to the size of the aggregates observed in the SEM images presented in Fig. S1. The size of individual nanoparticles could not be determined with DLS because of the limitation of the technique. However, the information obtained from DLS indicates that the aggregation of the suspension did not significantly change over the span of 18 weeks.

In addition, the Zeta potential was studied. Surface charges of the particles was studied using a Zetasizer (Malvern Zetasizer ZS90). Zeta potential (ζ) measurements were conducted on the same solutions as the ones used for size analysis. 0.75 mL of solution was pipetted into a Malvern zeta folded capillary cell (DTS1070), and placed inside the instrument. Program selections were identical to those chosen for size analysis. The sample values were tested and recorded for the determined optimal concentration (100-1000 kcps, 0.1 to 10 mS/cm). Three successive measurements within the range of optimal conditions were collected and averaged to determine the zeta potential. The Zeta potential remained fairly constant, despite a slight decay at week 18 (Fig. S9b).

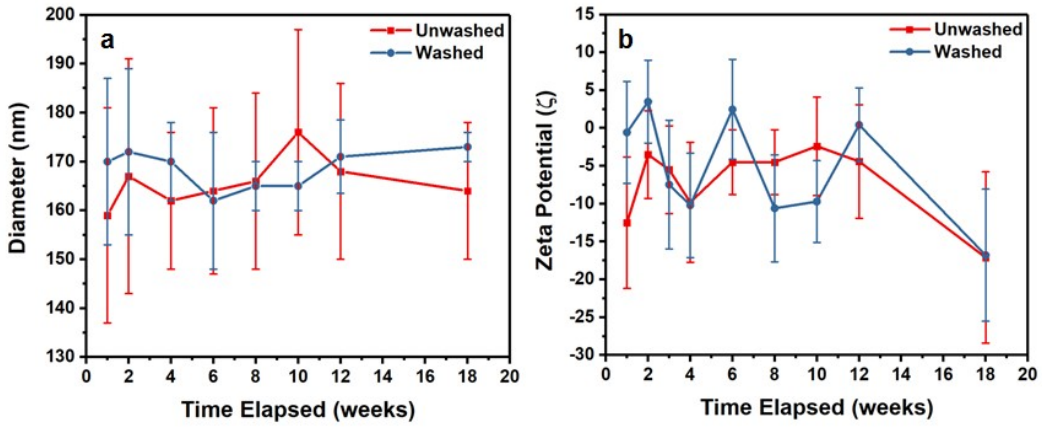

Figure S9. Effects of time and removing excess reagents on (a) diameter of ZnO agglomerated ZnO nanoparticles measured by DLS and (b) zeta potential. "Unwashed" refers to as-synthesized Zinkicide® while "washed" refers to the suspension of nanoparticles in water after the excess reagents were removed.

The evolution of the nanoparticle composition (as-synthesized (unwashed and ageing in reagents) and after removing excess reagents (washed ageing in water)) was evaluated by Raman spectroscopy, as shown in Fig. 6. The relative intensities of the hydrogen peroxide band (at 870 cm^{-1}) and water band (at 3410 cm^{-1}) were used to monitor changes in composition of the suspension over time. After removing excess reagents, a band at 840 cm^{-1} was observed in lieu of all the hydrogen peroxide bands. In this case, the evolution of the intensity of the zinc peroxide bond (at 840 cm^{-1}) with respect to the water band (at 3410 cm^{-1}) was monitored to study the evolution of the system. Fig. S10 presents the representative spectra that were used

to extract the ratio information presented in Fig. 6. The ratio was calculated by measuring the intensity of the bands from maximum to base of the band at the indicated wavenumbers.

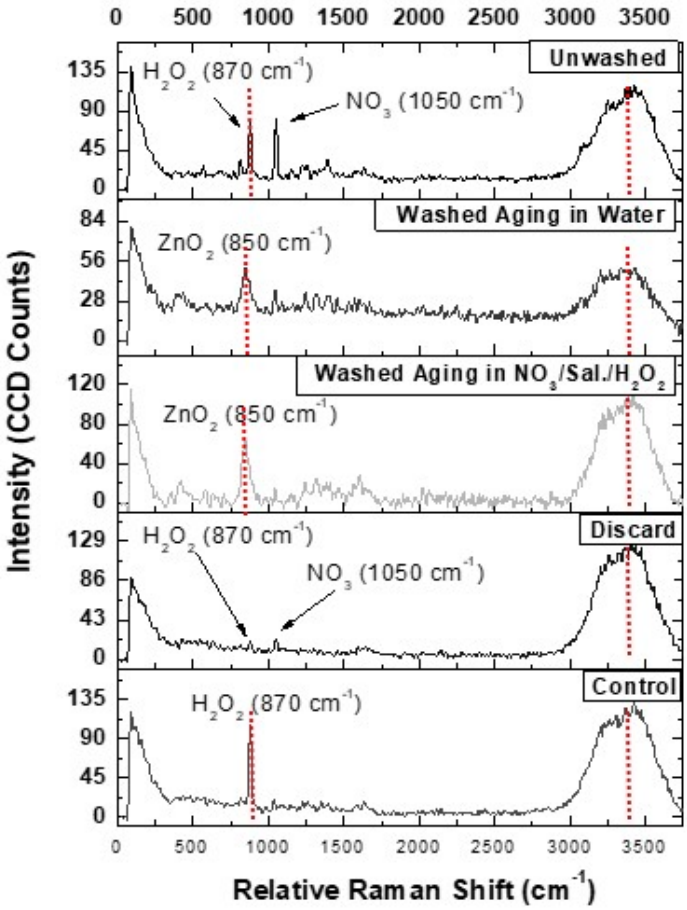

Figure S10. Raman spectra of unwashed (as-synthesized) and washed (in water) suspensions of Zinkicide® used to determine the hydrogen peroxide to water ratio zinc peroxide to water ratio plotted in Fig. 6.

Raman spectroscopy does not directly provide information on Zn. Hence, we complemented our study with AAS (Fig. S11). The Zn content in the Zinkicide® solution as-synthesized was determined for reference and confirmed on the 19000 μg/mL concentration. Next, Zn concentration was determined after each wash, for both the suspension with remaining nanoparticles and for the discard. Concentrations of 15000 μg/mL or higher were obtained for each measurement. The discards did not indicated concentration above a few hundred μg/mL. We note that the washing protocol can be imperfect due to the small size of the nanoparticles. Despite consistant difference in concentrations ranging from 19000 to ~15000 μg/mL, a non-statistically significant decay was observed between the washed solution obtained in week 1 and in week 12.

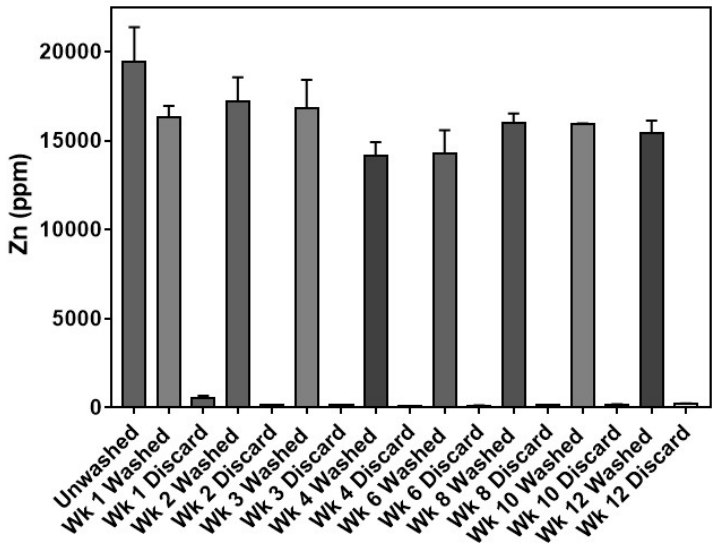

Figure S11. Quantification of Zn concentration by AAS in Zinkicide® as-synthesized (unwashed) suspension, Zinkicide® in water (washed) suspension after bi-weekly wash, and corresponding dicard.

Lastly, we evaluated the evolution of fluorescence properties of the nanoparticles over time. Fluorescence Lifetime Imaging Measurements (FLIM) were conducted as they provide information on the excited lifetime of the system. Fig. S12 presents a representative dataset of the fluorescence lifetime images collected on suspensions drop-casted onto a glass substrate. The fluorescence intensity and fluorescence lifetime were collected at every pixel. Lifetime curves were fitted with a double exponential function. The summary of fluorescence lifetime τ_1 and τ_2 are presented in Table S6 and a summary of the intensity is presented in Table S7. Reagents used to synthesize the nanoparticles do not exhibit any fluorescence. Thus, all values reported are attributed to the nanoparticles alone. As seen in Table S6, τ_1 and τ_2 remained below 9 ns in all measurements. The highest τ_1 and τ_2 were observed for measurements at week 1. The nanoparticles suspended in water (washed) exhibited higher τ_1 and τ_2 than nanoparticles in reagents (as-synthesized) (Table S6). After week 4, all τ_1 and τ_2 remained fairly constant, though fluorescence intensity was significantly lower than in week 1. Beginning at week 2, maximum laser power (800-850 nW) was required to collect sufficient counts/sec (Table S7), which was not the case in week 1. It is known that the excited lifetime can also be affected by defects on nanoparticle surfaces.

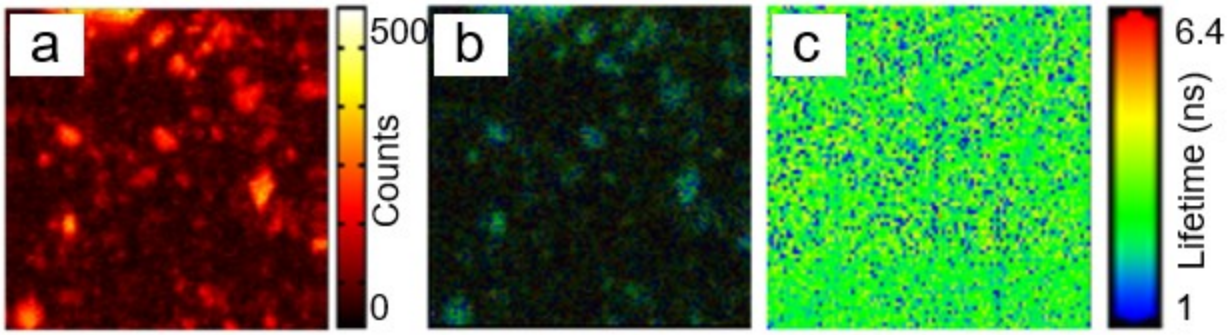

Figure S12. Fluorescent Lifetime imaging of Zinkicide® at Week 1. (a) Fluorescence intensity image of the unwashed solution. (b) Overlay of (a) and (c). (c) Fluorescence lifetime (FLIM) image of the unwashed solution.

Table S6. Fluorescence lifetime τ_1 and τ_2 and corresponding amplitudes A1 and A2 of the solutions.

* denoted samples that did not have fluorescent counts. N/A denotes samples that were not available at the current time due to processing time for solution settling.

Treatment		Week 1	Week 2	Week 4	Week 6	Week 8	Week 10	Week 12	Week 18
Zinkicide® as-synthesized	τ_1 A_1	1.9 26293	1.1 13052	1.1 14277	1.1 77521	1.1 68795	1.4 73791	1.2 54022	1.0 65570
	τ_2 A_2	6.4 6764	5.1 32669	4.8 29387	5.2 17806	5 15765	6.1 15510	5.4 12156	5 16894
Zinkicide® in water	τ_1 A_1	2.7 14669	1.1 125876	1.9 48895	1.1 62134	1.2 161912	1.3 109715	1.3 111458	1.3 94655
	τ_2 A_2	8.3 3198	4.9 26772	6.6 9910	5.2 14111	5.1 38651	5.6 25213	5.7 24660	5.6 22648
Discard	τ_1 A_1	*	*	*	*	*	*	*	*
	τ_2 A_2	*	*	*	*	*	*	*	*
Supernatant Zinkicide® as-synthesized	τ_1 A_1	N/A	N/A	1 36544	1.5 31836	1 21202	1.1 28501	1 37926	0.9 11435
	τ_2 A_2	N/A	N/A	4.5 5934	5.6 7753	4.7 4779	4.9 6187	5 37538	4.4 3195
Supernatant Zinkicide® in water	τ_1 A_1	N/A	N/A	*	*	*	*	*	*
	τ_2 A_2	N/A	N/A	*	*	*	*	*	*
Control	τ_1 A_1	*	*	*	*	*	*	*	*
	τ_2 A_2	*	*	*	*	*	*	*	*

Table S7. Fluorescence intensity in terms of the laser power applied and the intensity measured (cts/s).

* denoted samples that did not have fluorescent counts.

Treatment		Week 1	Week 2	Week 4
Zinkicide® as-synthesized	Power applied (nW)	150	90	850
	I (cts/s)	4000-5000	3000-6000	4000-5000
Zinkicide® in water	Power applied (nW)	300	150	850
	I (cts/s)	3500-5000	3000-6300	2700-4100
Discard	Power applied (nW)	800	850	850
	I (cts/s)	600-2000	500-600	800-1000
Supernatant Zinkicide® in water	Power applied (nW)	*	*	*
	I (cts/s)	*	*	*
Control	Power applied (nW)	800	800	850
	I (cts/s)	100-300	0-100	0-50

References

1. Santra S, Berroth M, inventorsCompositions including a vacancy-engineered (VE)-ZnO nanocomposite, methods of making a composition , method of using a composition. US2018.
2. https://edis.ifas.ufl.edu/cg040 [
3. https://www.fdacs.gov/Divisions-Offices/Plant-Industry/Pests-Diseases/Citrus-Pests-and-Diseases/HLB-Citrus-Greening; https://edis.ifas.ufl.edu/topic_citrus_greening [
4. Ilavsky J, Jemian PR. Irena: tool suite for modeling and analysis of small-angle scattering. Journal of Applied Crystallography. 2009;42(2):347-53.
5. Beaucage G. Approximations Leading to a Unified Exponential/Power-Law Approach to Small-Angle Scattering. Journal of Applied Crystallography. 1995;28(6):717-28.
6. Beaucage G. Small-Angle Scattering from Polymeric Mass Fractals of Arbitrary Mass-Fractal Dimension. Journal of Applied Crystallography. 1996;29(2):134-46.
7. Philip D, John A, Panicker CY, Varghese HT. FT-Raman, FT-IR and surface enhanced Raman scattering spectra of sodium salicylate. Spectrochimica Acta Part A: Molecular and Biomolecular Spectroscopy. 2001;57(8):1561-6.
8. Volod'Ko L, Huoah L. The vibrational spectra of aqueous nitrate solutions. Journal of Applied Spectroscopy - J APPL SPECTROSC. 1968;9:1100-4.
9. Pettersson M, Tuominen S, Räsänen M. IR Spectroscopic Study of H2O2, HDO2, and D2O2 Isolated in Ar, Kr, and Xe Matrices. The Journal of Physical Chemistry A. 1997;101(6):1166-71.
10. Monkhorst HJ, Pack JD. Special points for Brillouin-zone integrations. Phys Rev B. 1976;13(12):5188-92.
11. Baroni S, De Gironcoli S, Dal Corso A, Giannozzi P. Phonons and related crystal properties from density-functional perturbation theory. Reviews of Modern Physics. 2001;73(2):515.
12. de Gironcoli S. Lattice dynamics of metals from density-functional perturbation theory. Phys Rev B Condens Matter. 1995;51(10):6773-6.
13. Rawal TB, Ozcan A, Liu S-H, Pingali SV, Akbilgic O, Tetard L, et al. Interaction of Zinc Oxide Nanoparticles with Water: Implications for Catalytic Activity. ACS Applied Nano Materials. 2019;2(7):4257-66.

14. Lakshmi Prasanna V, Vijayaraghavan R. Insight into the Mechanism of Antibacterial Activity of ZnO: Surface Defects Mediated Reactive Oxygen Species Even in the Dark. Langmuir. 2015;31(33):9155-62.
15. Espitia PJP, Soares NdFF, dos Reis Coimbra JS, de Andrade NJ, Cruz RS, Medeiros EAA. Zinc oxide nanoparticles: synthesis, antimicrobial activity and food packaging applications. Food and bioprocess technology. 2012;5(5):1447-64.
16. Xie Y, He Y, Irwin PL, Jin T, Shi X. Antibacterial activity and mechanism of action of zinc oxide nanoparticles against Campylobacter jejuni. Appl Environ Microbiol. 2011;77(7):2325-31.
17. Tayel AA, EL-TRAS WF, Moussa S, EL-BAZ AF, Mahrous H, Salem MF, et al. Antibacterial action of zinc oxide nanoparticles against foodborne pathogens. Journal of Food Safety. 2011;31(2):211-8.
18. Lamprou DA, Smith JR. Applications of AFM in pharmaceutical sciences. Analytical Techniques in the Pharmaceutical Sciences: Springer; 2016. p. 649-74.
19. Nishino T, Ikemoto E, Kogure K. Application of atomic force microscopy to observation of marine bacteria. Journal of oceanography. 2004;60(2):219-25.
20. Wright CJ, Shah MK, Powell LC, Armstrong I. Application of AFM from microbial cell to biofilm. Scanning. 2010;32(3):134-49.
21. Shang L, Wang Y, Jiang J, Dong S. pH-dependent protein conformational changes in albumin: gold nanoparticle bioconjugates: a spectroscopic study. Langmuir. 2007;23(5):2714-21.
22. Lynch I, Dawson KA. Protein-nanoparticle interactions. Nano today. 2008;3(1-2):40-7.
23. Xiao Y, Liu Y, Zhang W, Qi P, Ren J, Pei Y, et al. Formation, Structure, and Mechanical Performance of Silk Nanofibrils Produced by Heat-Induced Self-Assembly. Macromolecular Rapid Communications.n/a(n/a):2000435.
24. Zhong J, Liu Y, Ren J, Tang Y, Qi Z, Zhou X, et al. Understanding Secondary Structures of Silk Materials via Micro- and Nano-Infrared Spectroscopies. ACS Biomaterials Science & Engineering. 2019;5(7):3161-83.